Effect of isolation on two-particle correlations in pilot-wave hydrodynamics

André Nachbin*
Instituto de Matematica Pura e Aplicada, IMPA, Estr. Dona Castorina 110, Rio de Janeiro, RJ 22460-320, Brazil

(Received 11 March 2022; accepted 17 August 2022; published 16 September 2022)

We present a numerical investigation on the effect of isolation imposed on two previously correlated walking droplets. These two bouncing droplets oscillate horizontally, confined to separate cavities placed at a distance. Nachbin [Chaos **28**, 096110 (2018)] showed that the droplets are coupled through the underlying wave field of the multicavity system, resulting in nonseparable subsystems: their respective probability distributions cannot be inferred through an individual solitary droplet. Beyond correlated, the droplets are statistically indistinguishable, highlighting their intrinsically related statistics. Isolation is imposed through a wide barrier which abruptly halts the long-range wave-mediated interactions between droplets. Shortly after, both droplets transition to new cycles in phase space. The postisolation phase-space histograms reflect new and effectively identical probability density distributions. The particles' new energy level is higher than if the droplets had been isolated at all times. The new energy level observed, and sustained beyond isolation, is shown to be related with long-range disturbances existing prior to isolation. The postisolation change of phase-space cycles is faster than any possible propagation of information between subsystems. The statistical droplet pairing is therefore associated to preexisting correlations between particles. The intrinsic statistical relation of the bipartite system adjusts itself to new configurations where statistical indistinguishability persists even after the particles are set into isolation.

DOI: 10.1103/PhysRevFluids.7.093604

I. INTRODUCTION

The groundbreaking discovery by Couder and Fort *et al.* [1,2] led to many works on the pilot-wave hydrodynamic, as first reviewed by Bush [3] in 2015 and further reviewed by Bush and Oza [4] in 2021. Pilot-wave hydrodynamics originates from bouncing droplets of silicon oil that can levitate over a vibrating bath of the same fluid and be self-propelled by the Faraday waves it generates. Following Couder and Fort, these walking droplets are viewed as a hydrodynamic quantum analog of a wave-particle system. For this reason, since 2018 this class of problems has been called HQA [5]. These walking droplets represent a macroscopic example of wave-particle duality and serve as the basis for the field of HQAs.

Before describing our results, we digress on quantum mechanics–related terminology which needs to be introduced and interpreted for this classical system. At the Introduction of their review article, Horodecki *et al.* [6] mention that in quantum mechanics one has the "existence of global states of a composite system which cannot be written as a product of the states of individual subsystems." These are statistical states, and a product of states implies independence. We adopt this definition for *nonseparability*. According to Werner [7], saying that the expectation value for the joint measurement of observables on the respective subsystems always factorizes means

*nachbin@impa.br

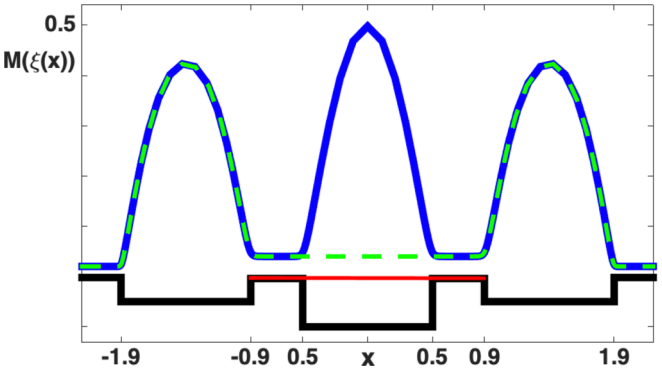

FIG. 1. The interconnected three-cavity system is depicted through a thicker polygonal profile. Droplets are subsequently isolated into two well-separated cavities. As indicated by the thinner line, a wide barrier is located at $x \in [-0.9, 0.9]$, establishing a shallow region of depth $h_b = 0.04$ cm. The metric coefficient $M(\xi(x))$, which controls the wave propagation speed, is graphed above the cavity profiles. The dashed profile corresponds to the isolated case where the wave speed is small over the wide barrier. In the mathematical model the nonsmooth variable geometry along the bottom is equivalent to the smooth variable coefficient $M(\xi(x))$ along the free surface.

that we are simply conducting two separate experiments at the same time. Hence the classical multiplication rule for probabilities applies [7]. Schrödinger called "entanglement" the state of a composite systems which "underlines the *intrinsic statistical relations* between particles of a compound quantum system" [6]. In the quantum literature nonseparable (or inseparable) states often refer to entangled global states. Henson [8] discusses at length that nonseparability should be used in the more general sense, as in the above statement by Horodecki *et al.*, and therefore we adopt this definition which precedes establishing entanglement.

The present wave-particle model is not from quantum mechanics. Throughout this article, as was done in [9] and mentioned above, we consider having nonseparable states when a droplet's statistics cannot be obtained through an isolated individual subsystem. Furthermore, we understand that HQA nonseparability infers that both droplets' *statistics are intrinsically related* in the sense that there is an internal mechanism controlling the bipartite correlations and producing a *special underlying structure*. For quantum particles this special structure gives rise to nonclassical correlations and entanglement. Nonclassical Einstein-Podolsky-Rosen (EPR) correlations and entanglement are quantified by violating Bell's inequality [7,10] or equivalently, the Clauser-Horne-Shimony-Holt (CHSH) inequality (see [6], p. 877) under certain conditions, such as having photons spacelike separated. As an example, consider the intrinsically related spin statistics due to a singlet state in the EPR experiment [7,10]: if one particle is very likely to be spin-up, then the other is very likely to be spin-down.

HQA bipartite nonseparability has been presented through the statistical indistinguishability of two droplets [9] placed at a distance. Droplets are confined to the two extremes cavities depicted in Fig. 1. The geometry of the midcavity is designed to enhance the long-range interaction between the two bouncing droplets, which oscillate horizontally while trapped within their respective cavities. It was shown that the dynamics of an individual subsystem does not lead to the same (numerical) probability density function (PDF) as when the dynamics is considered with the entire composite system. For the composite system both droplets display identical histograms in phase space. The time evolution of the histograms is not symmetric but end up converging to being identical at the end of a long enough simulation. This internal statistical synchronization was our first example of an intrinsically related correlation between the two droplets.

The intrinsic statistical behavior of a bipartite walker system was further explored by Papatryfonos *et al.* [11] through a display of uncertain but cooperative tunneling. The fluid domain now

comprises five cavities: an intervening deep cavity with two cavities on either side constitutes the respective subsystems. Using the intervening midcavity to tune long-range correlations, Papatryfonos *et al.* design two-level subsystems for each droplet. Each cavity of each subsystem is at a different energy level. The droplet can tunnel between the two cavities of their respective subsystem. The two energy-level cavities create a metastable double-well potential for each particle. The time of residence in the higher-energy well is much shorter than that in the ground state, namely, the cavity where the droplet is trapped for longer time intervals before tunneling. Papatryfonos *et al.* [11] discovered a classical system where cooperative tunneling of the bipartite system exhibits super- or subradiance. Through long-range interactions the probability of tunneling can be enhanced by the presence of the other droplet. These findings hint at the plausibility of developing hydrodynamic analog Bell tests [12] and the first establishment of a hydrodynamic analog of quantum entanglement.

Having the above in perspective, the present paper investigates the persistence of statistical indistinguishability, even after the two subsystems are isolated by the sudden appearance of a large barrier. This investigation is motivated by the well-known (1935) Einstein-Podolsky-Rosen *gedanken experiment*. Aspect *et al.* [10] (1982) reported their experiment where a source first emits a pair of photons (a singlet) in a similar nonfactorizing state. Then, after the particles have been separated, quantum mechanics predicts correlated measurements on the two particles. In the present work we perform computational simulations inspired by the above setup. In order to isolate the droplets after a preliminary interaction, a wide barrier suddenly appears in between them at a prescribed time. Surprisingly, nonseparability and the intrinsically related correlations are persistent even after the bipartite system is brought into isolation. It is shown that upon isolation, the bipartite system quickly migrates to new and identical probability density distributions. These new PDFs are different from those had the droplet been isolated at the onset. The (postisolation) statistical PDF transition is faster than any possible propagation of information between subsystems, namely, faster than the phase speed of wave modes generated by the bouncing droplets. A detailed phase-speed analysis is presented in the Appendix. It is also surprising that the long-range pilot-wave modes, after adapting to the new isolating topography, are not dissipated. The droplets' statistical indistinguishability persists beyond the time they were communicating.

II. THE MATHEMATICAL MODEL FOR DROPLET ISOLATION

Regarding the fluid dynamics modeling, to be presented, the bouncing droplet model balances dissipation, due to viscosity, against the forcing due to the vertical shaking of the fluid bath. A multicavity topography, such as that presented in Fig. 1, is designed to enhance long-range correlations. Different midcavity depths (or widths) can affect the long-range interactions [9]. In some cases the bipartite dynamics gives rise to a spontaneous Kuramoto-like synchronization [13], displaying phase-locked droplets oscillating laterally while trapped within cavities. Generalizing the Kuramoto model, Nachbin [9] reported a new type of oscillator coherence where droplets would exhibit statistical indistinguishability rather than phase locking. Two droplets traverse a similar orbit in phase space, seemingly in an unrelated fashion, but display identical numerical probability density distributions, evident through their respective histograms.

A. Background

The hydrodynamic pilot-wave system is an object that was not imagined to exist in classical mechanics, namely, an object that in association with a droplet has dynamical properties of both a particle and a wave. The dynamics of the wave-particle association is highly nontrivial, as shown in the present article. Therefore laboratory and numerical findings foster further theoretical developments. The Faraday waves generated by a certain number of droplet bounces yields a bath with the system's memory [4,14]. These Faraday surface waves are generated just below the Faraday instability threshold. The droplet-generated waves are governed by a system of partial differential

equations (PDEs) through a weakly viscous, linear quasipotential theory [15]. This set of wave equations along the free surface is coupled to a trajectory equation for each droplet. The trajectory equation arises from Newton's law as a weakly damped mass-spring-type ordinary differential equation (ODE). The feedback between wave and droplet is highly nonlinear and takes place through the forcing terms of both systems of differential equations.

The fluid under consideration is silicon oil, where surface tension and viscous effects play a role. The wave model used here was obtained from a systematic asymptotic reduction of the Navier-Stokes equations [15] and then further simplified to a one-dimensional (1D) hydrodynamic pilot-wave model [16] in a confined domain with cavities. The wave model is formulated in the frame of the fluid bath oscillating vertically at frequency ω_0. The vertical acceleration is taken as $g(t) = g[1 + \Gamma \sin(\omega_0 t)]$, where g is the gravitational acceleration and Γ the forcing amplitude. The fluid is quiescent for $\Gamma < \Gamma_F$, where Γ_F is the Faraday threshold. A subharmonic instability takes place when $\Gamma \geqslant \Gamma_F$ [4,17]. Prescribed by the water-wave dispersion relation [17], standing Faraday waves arise with wavelength λ_F. A bouncing droplet can trigger these waves when $\Gamma < \Gamma_F$. Couder and coauthors [1,2] discovered the walking droplet when the parameter Γ exceeds (what was called) the walking threshold Γ_w [3]: $\Gamma_w \leqslant \Gamma < \Gamma_F$. The droplet is then guided by its underlying pilot wave, a spatially extended (modulated) monochromatic wave field with a Faraday period $T_F = \omega_0/2$ [17].

B. Formulation of the wave model

The present mathematical model is based on a two-dimensional, weakly viscous quasi-potential fluid model [15]. The waves are one-dimensional, along the top boundary of the two-dimensional (2D) fluid region. A reduced 1D wave model has been used for tunneling simulations [16], as well as for the study of two droplets correlated at a distance [9,11]. As the main mathematical ingredient, a Fourier integral operator, is constructed to analytically reduce the 2D problem to a 1D wave problem along the undisturbed free surface. The 1D Fourier integral, a Dirichlet-to-Neumann (DtN) operator, has information encoded in its symbol (or multiplier) ensuring that the underlying function of interest satisfies Laplace's equation, in the 2D fluid body, and a homogeneous Neumann condition along the polygonal-shaped (impermeable) bottom, describing the respective cavity system. The novelty in the present formulation is that through the DtN operator we can instantaneously change the cavity structure. Therefore we can isolate the droplets at a prescribed instant in time. The wave-particle system of equations is now described. We begin with the wave equations.

Let the wave elevation be defined as $z = \eta(x, t)$ and the velocity potential by $\phi(x, z, t)$. The velocity field, in the bulk of the fluid associated to this harmonic function, is given by $(u, v) = \nabla\phi$. As presented in [15], after a Helmholtz decomposition, the potential ϕ is associated with the incompressible and irrotational component of the flow. The fluid has density ρ, surface tension σ, and kinematic viscosity ν. The free surface wave equations, at $z = 0$, are given by [15,16]

$$\frac{\partial \phi}{\partial t} = -g(t)\eta + \frac{\sigma}{\rho}\eta_{xx} + 2\nu\,\phi_{xx} - \frac{1}{\rho}\sum_{j=1,2} P_d(x - X_j(t)), \tag{1}$$

$$\frac{\partial \eta}{\partial t} = DtN[\phi] + 2\nu\,\eta_{xx}. \tag{2}$$

The Bernoulli law displays the presence of each droplet through the pressure terms P_d. This is a pressure-based wave-making term, which acts over an interval equal to the droplet's diameter and centered at $X_j(t)$, the droplet's position in time. These pressure terms are activated periodically only for a fraction of the Faraday period T_F. In the kinematic condition, the DtN operator maps the Dirichlet data $\phi(x, 0, t)$ onto the free surface's normal speed, at every time t:

$$DtN[\phi] = \phi_z(x, 0, t). \tag{3}$$

The representation of this operator in the physical domain is highly nontrivial. Hence one has to map the fluid domain onto a simpler computational domain. This is achieved through a conformal mapping.

Conformal mapping plays an important role in the mathematical modeling and in the numerical scheme. The vertical structure of the flow is encoded in a Fourier integral operator, namely, a Dirichlet-to-Neumann operator. To construct this operator, the nonsmooth polygonal-shaped bottom, namely, the cavities, is mapped onto a flat bottom by using a numerical Schwarz-Christoffel mapping [18].

The Schwarz-Christoffel mapping [18] performs the conformal transformation from a uniform strip of unit height onto our undisturbed physical domain. The water-wave problem is linear, and therefore the free surface conditions can be applied at the undisturbed level. Hence the physical domain to be mapped is fixed in time. The uniform strip is defined in the complex w plane, where $w = \xi + i\zeta$. The physical domain is in the complex Z plane, where $Z = x + iz$. The complex function $Z = F(w)$ defines the map. The undisturbed free surface $z = 0$ has as a pre-imagem $\zeta = 1$, which is the convention in the SCHWARZ-CHRISTOFFEL TOOLBOX [18]. The Jacobian of this change of variables is given as $|J| = |dZ/dw|^2$. Along the free surface, $|J|(\xi) = z_\xi^2(\xi, 1)$. Using the Cauchy-Riemann equations [19], it follows that

$$\phi_\zeta(x, 0) = \phi_z z_\zeta. \tag{4}$$

We call $M(\xi) \equiv z_\zeta(\xi, 1)$ the metric coefficient, which is obtained as the square root of the Jacobian, evaluated along the free surface.

In the canonical domain denote the Dirichlet data as $\varphi(\xi, t) = \phi(x(\xi, 1), 0, t)$. The Fourier representation, regarding the canonical variable ξ, is given by

$$\varphi(\xi, t) = \frac{1}{\sqrt{2\pi}} \int_{-\infty}^{\infty} \hat{\varphi}(k, t) e^{ik\xi} dk.$$

In the w plane the DtN operator is easily computed [16] as

$$\phi_\zeta(\xi, 1, t) = \frac{1}{\sqrt{2\pi}} \int_{-\infty}^{\infty} [k \tanh(k)] \hat{\varphi}(k, t) e^{ik\xi} dk. \tag{5}$$

The Fourier symbol is defined in brackets. This leads to a straightforward computation using the FFT (fast Fourier transform). By combining expressions (3)–(5), we have the DtN operator in the physical domain:

$$DtN[\phi](x, t) = \frac{1}{M(\xi(x, 0))} \phi_\zeta(\xi, 1, t). \tag{6}$$

The function $\xi(x, 0)$ is important in mapping a uniform grid in the physical domain to a nonuniform grid in the canonical domain. Interpolation is used to get function values on a uniform grid in the canonical domain and thus perform an FFT. Both the regridding function $\xi(x, 0)$ and the metric coefficient $M(\xi)$ are readily available through the SCHWARZ-CHRISTOFFEL TOOLBOX. A few useful commands are provided in Fokas and Nachbin [20].

In Fig. 1 we superimpose two different profiles for the cavity system. One has three cavities, with a deep one in the middle. The other profile displays the two extreme cavities isolated by a very wide barrier, extending over the interval $[-0.9, 0.9]$. The respective metric coefficient $M(\xi(x, 0))$ is displayed over the cavity profiles. We have performed the numerical conformal mapping for each case. Let us denote the mapping for the three-cavity system as $Z = F_1(w)$ and for the isolated system by $Z = F_2(w)$. Respectively we have two metric coefficients. The solid line depicts $M_1(\xi(x, 0))$, while the dashed line depicts $M_2(\xi(x, 0))$. By using the DtN formulation, the nonsmooth cavity geometries have been mathematically replaced by these smooth variable coefficients (M_j) along the kinematic condition, having in mind expression (6).

The results here presented display the effect of setting the droplets into isolation after they have experienced some mutual interaction at a distance. The goal is to study the effect of isolation on correlations that have been established. Having this in mind, one sets a time for which the mapping function F_1 is replaced by F_2, producing the relevant variable coefficients. We will present simulations where the cavity geometry is abruptly changed, enabling the droplets to first interact

and then to go into isolation. Numerically, this is executed by computing expression (6) twice. We will contrast these results with those where the droplets are isolated at the onset of the simulation.

A brief remark adds to the physical intuition of our modeling. As shown in [16], for clarity, it is instructive to momentarily disregard the droplet, the bath shaking, and the effect of surface tension. By considering the long-wave limit, the cavity structure (encoded in the DtN operator) asymptotically corresponds to a variable wave speed. In other words, the above simplifying assumptions yield a wave equation, for the Dirichlet data φ, of the form

$$\varphi_{tt} - g[M(\xi(x,0))\varphi_x]_x = 0. \tag{7}$$

When taking into account all the ingredients, the wave-droplet dynamics is definitely more complex. But qualitatively, the DtN operator accounts for the variable wave speed, thus having information of the fluid body's vertical structure. At the moment of the droplet isolation, suddenly the wave propagation speed is dramatically diminished in the region of the wide barrier.

C. The droplet model

The wave system presented above is coupled to the droplet's horizontal trajectory equation, through its forcing term:

$$m\frac{d^2X_j}{dt^2} + 0.01\,G(t)\frac{dX_j}{dt} = -G(t)\frac{\partial\eta}{\partial x}(X_j(t),t), \tag{8}$$

with $j = 1, 2$ indicating each droplet's motion under Newton's law. These droplet equations are coupled among themselves through the underlying wave field $\eta(x,t)$. The coupling is implicit, since X_2 does not appear in X_1's equation and vice versa. The slope of the wave elevation provides the droplet forcing and represents the pilot wave that guides the particle. The magnitude of this propulsive force during contact time, here prescribed as $Tc = T_F/4$, is denoted by $G(t)$. This coefficient depends on surface tension and also appears in the damping coefficient. Further modeling details are given in [15,16].

For the numerical simulations we consider the physical domain as being long enough so that we have quiescent conditions at the ends and therefore impose a periodic boundary condition. As a consequence, the spatial derivatives of Eqs. (1), (2), and (8) are computed using a Fourier spectral method. As mentioned regarding the conformal mapping, commands are readily available in Fokas & Nachbin [20] to compute the Jacobian as well as $\xi_j = \xi(x_j, 0)$ on a given grid. The time evolution is performed with a second-order fractional-step Verlet method.

III. RESULTS

The physical parameters used in the present study are the same as in Milewski *et al.* [15]: the droplet radius is $R_o = 0.035$ cm, the surface tension coefficient is $\sigma = 20.9$ dyn cm^{-1}, the kinematic viscosity is $\nu = \mu/\rho = 0.16\,\text{cm}^2\,\text{s}^{-1}$, the fluid density is $\rho = 0.95$ g cm^{-3}, and the forcing (angular) vibrational frequency is ω_o, corresponding to 80 Hz. The respective Faraday wavelength that arises is $\lambda_F \approx 0.47$ cm. We adopt boundaries comparable to those examined in the laboratory: adjacent to the main cavity is a shallow region that eliminates the meniscus on the sidewalls that would otherwise arise.

Figure 2 displays our first simulation, which considers a milder cavity change. The midcavity depth has a nontrivial depth change at time $t = 250T_F$ but not strongly affecting the oscillators. The midcavity is suddenly reduced to one-third of its original depth. As explained in the previous section, the sudden cavity change is mathematically performed by substituting the conformal mapping's Jacobian by another Jacobian. This impacts the variable coefficient of the wave equation, which controls the wave speed. In Fig. 2 we start the simulation with the same configuration as in Nachbin [9], where the droplets performed nontrivial cycles in phase space and are nearly synchronized most of the time. At time $t = 250T_F$ the midcavity depth is reduced from 3 to 1 cm. The wave pattern

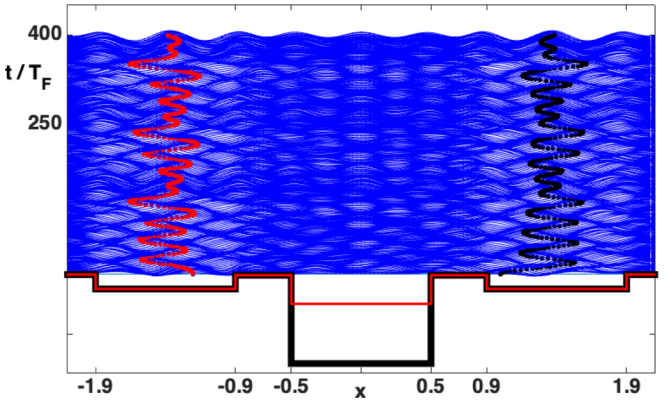

FIG. 2. The time evolution of the 1D droplet dynamics. Time evolves in the vertical direction. The shaking strength is at $\Gamma = 4.8$. The droplets are initially located at $x = -1.20$ in the left cavity and at $x = 1.0$ in the right cavity. The traces for the droplet evolution in time are represented by the red and black dots, respectively. Both cavities are of depth $h = 0.5$ cm and width $L = 1.0$ cm. The depth over the barriers is $h_b = 0.04$ cm. The barrier width is equal to 0.4 cm. At time $t = 250T_F$, the midcavity depth is reduced from 3 to 1 cm, as indicated by the thinner (red) polygonal line. The particle dynamics and the wave pattern are not strongly affected by the sudden change in this three-cavity system.

over the midcavity is not strongly altered. There is still an indication of information flowing in both directions, mediated by the wave field occupying the entire domain. The range of the traces in time, for each droplet, is not strongly affected. A stronger impact will be observed when the midcavity is removed.

A. Isolating droplets in a three-cavity system

To contrast with the above simulation, consider two droplets isolated at the onset, as displayed in Fig. 3. A long shallow barrier is shown along $x \in [-0.9, 0.9]$. The shaking strength Γ and initial droplet positions are the same as in Fig. 2. It is clearly seen that there is negligible wave activity over the barrier region. The isolated droplets adjust themselves to the center of their cavities and

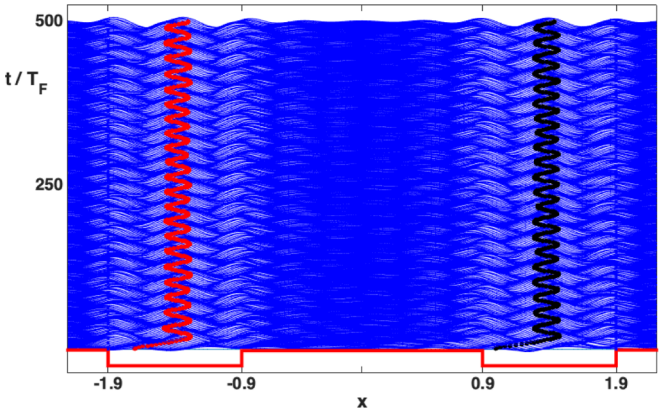

FIG. 3. The two cavities are well separated by the wide barrier along $x \in [-0.9, 0.9]$. The shallow region is of depth $h_b = 0.04$ cm. The droplets perform small amplitude oscillations. The wave field over the barrier region is nearly nonexistent, indicating that the two subsystems are effectively uncorrelated.

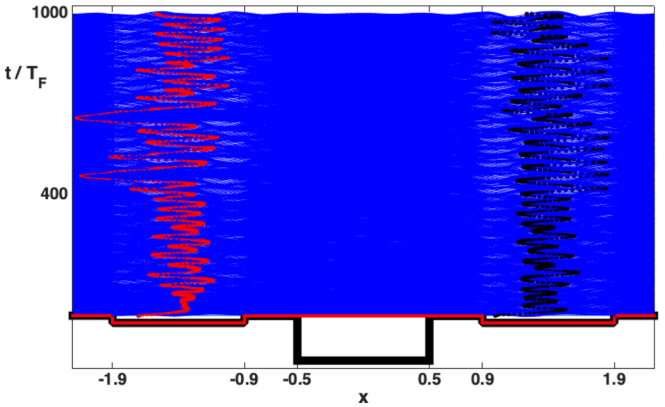

FIG. 4. Up to time $t = 400T_F$ the droplets are in the integrated three-cavity system, when suddenly the midcavity is removed and replaced by the wide barrier. In contrast to that observed in Fig. 3, the system does not decay to the smaller amplitude regime observed previously. Both droplets quickly transition to a higher energy level, with oscillations over a wider range, and sustained beyond isolation in a manifestation of information stored in the wave field prior to the cavity removal.

perform harmoniclike oscillations of small amplitude. When droplet isolation is imposed after they have experienced some prior wave-mediated communication, the resulting dynamics is strikingly different from that of Fig. 3. At time $t = 400T_F$ the midcavity is removed, and a wide shallow barrier of depth 0.04 cm is placed in between the two remaining cavities. Beyond isolation, the oscillators quickly transition to the same higher energy level, as shown in Fig. 4. As clearly seen, both droplets quickly expand their range of oscillation within their respective cavities. As will be shown below, it is striking that upon isolation both droplets transition from identical probability distributions to another pair of identical probability distributions. This is expressed through their histograms in phase space. The transition takes place faster than any possible signaling between the two extreme cavities. The Appendix contains details of this transition.

The phase-space dynamics, for three different cases, is depicted in Fig. 5. The darker (black) limit cycle, at the center, is related to the dynamics of the droplets isolated at the onset (Fig. 3). We point out that the contact times have been removed from the graphing, for a better visualization through smooth cycles, as was done in some cases in [9,21]. We note that during the contact time the droplet is accelerated by the underlying wave and therefore generates a spike in their phase-plane orbits, as shown in more detail in Nachbin [9,21]. Surrounding the well-defined harmoniclike limit cycle (black curve; figure 5) we display the slightly wider (blue) orbits for the case of the nearly synchronized droplets presented in Nachbin [9]. Their wider range is due to the deep midcavity being (locally) in a nearly resonant regime, namely, being closer to the Faraday threshold [9,21] and therefore better extracting energy from the vertical shaking (i.e., the external forcing). Not only is the midcavity an efficient source of wave energy, through the Faraday mechanism, but it also amplifies signals being emitted by the droplets at the ends of the domain [9,21]. In the absence of this amplification mechanism, namely, without the midcavity at the onset, viscous dissipation dominates and damps the wave-mediated coupling at a distance. As seen, the wide barrier is effective in isolating the droplets. The colored thinner curves in Fig. 5 depict several orbits when the cavity system is abruptly changed. Before isolation the orbits are identical to the nearly-in-synch case (in blue) just discussed. Beyond isolation the oscillation range increases and covers a larger area, approximately within the interval [1, 1.8]. Three colors are used to display simulations with three different times of isolation: $t = 320T_F$, $400T_F$, and $550T_F$. The outcome is effectively the same, independent of when isolation takes place. Prior to isolation, when long-range interaction takes place, bipartite information is stored in the underlying wave field, which has transmitted information

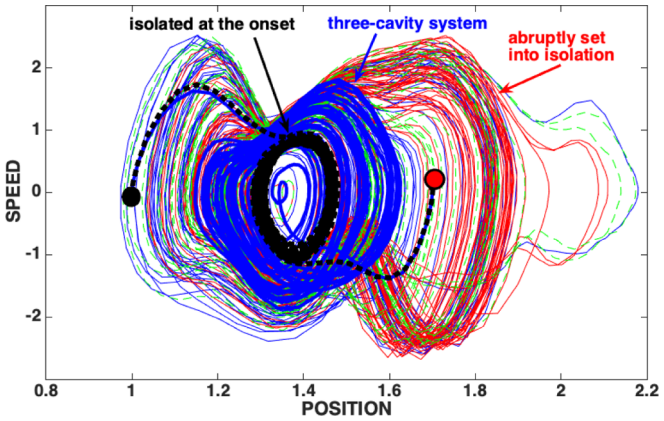

FIG. 5. Phase-space dynamics. The small cycle in the center (black) is related to Fig. 3, where the droplets were isolated at the onset. The slightly wider set of cycles (blue) is related to the three-cavity system, where there is a mutual droplet influence at a distance. The cycles with the largest range in phase space, and therefore at a higher energy level, refer to three different cases where the droplets were abruptly set into isolation at three different times: red at $t = 320T_F$, dashed green at $t = 400T_F$, and blue at $t = 550T_F$. The latter case ran up to $t = 1500T_F$ with a different initial condition from the others, and the higher-energy phase dynamics was sustained for all times beyond isolation.

through the nearly resonant midcavity. Note that independent of the isolation time used, the new (higher) energy level is the same and persistent.

In Fig. 6 we present the most striking result for this bipartite system. The simulation is for a similar setup as Fig. 4 but for a longer time interval. The particles are viewed in phase space, and the respective histograms are numerically constructed, indicating the regions where we are most likely to find these droplets. The top histogram is for the left droplet, and it has been reflected to the positive axis for a better comparison with the next histogram, which is for the right droplet. Their positions and speeds have been binned in phase space up to the time of isolation ($t = 2000T_F$). This is the case where the particles are nearly synched, looping over several cycles of varying amplitudes (radii). After isolation this phase coherence is lost and the spontaneous synchronization is not observed. Nevertheless, both droplets quickly transition to new and identical probability distributions, as indicated by the two histograms in the lower part of Fig. 6. This quick transition is discussed in more detail in the Appendix. Again, the histogram for the left particle [(C); third from top to bottom] has been reflected for comparison purposes. Note that their spatial range has increased by a nontrivial amount. This is a striking evidence of information being stored in the wave field during the preisolation dynamics. As discussed in the Appendix, the transition of probability distributions is faster than any possible signaling time between the extreme cavities. Calculating the Fourier content of the pilot wave (see Appendix) and the modes' respective phase speeds shows that trajectory deviations in phase space are revealed faster than any possible signaling. The key ingredient is the perseverance and adjustment of long-range correlations, beyond particle isolation, in the background vibrational field [22]. Understanding the role of these correlations and its related modes is a topic of interest and of future study with collaborators. It is important to stress that even in the presence of viscous dissipation and of a higher impedance to propagation, the (postisolation) configuration space for these particles is sustained thereafter, not decaying to the lower energy level when isolation was imposed at the onset (Fig. 3).

In order to have a better intuition on the unexpected dynamics that follows the sudden removal of the midcavity, we now discuss Figs. 7 and 8. At the top of Fig. 7, the wave elevation, related to Fig. 3, is displayed for a short time interval ($t \in [100T_F, 180T_F]$). The wave field regards the case where the two droplets are isolated at the onset by the wide barrier. At the bottom of Fig. 7, the wave elevation,

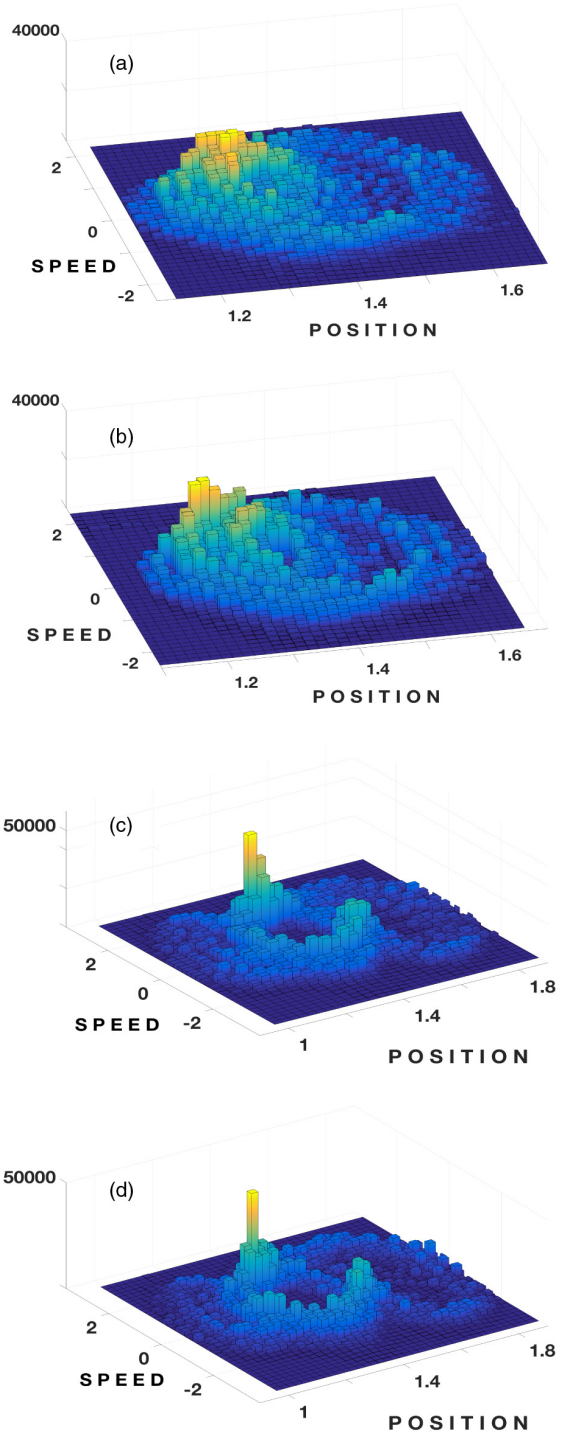

FIG. 6. Histograms in phase space related to a longer run done in the same geometry as Fig. 4. Top two histograms: left (a) and right (b) droplet up to the isolation time $t = 2000T_F$. Bottom two histograms: left (c) and right (d) droplet after isolation and up to time $t = 4000T_F$. After isolation new and identical distributions arise.

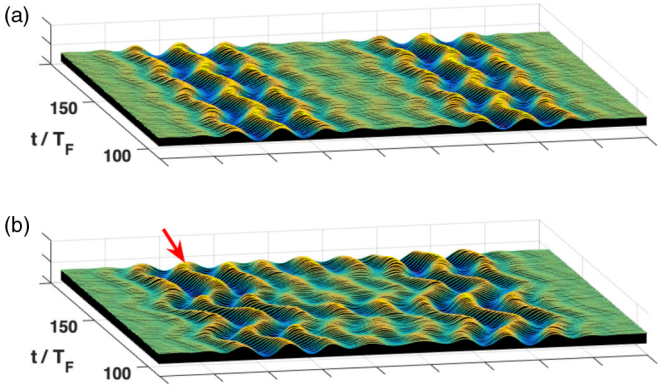

FIG. 7. The top graph (a) presents the wave evolution in time from Fig. 3, where the droplets were isolated from the onset. The wave field is displayed in the time interval $t \in [100T_F, 180T_F]$. We see the wave activity in the region of the two side cavities and a nearly quiescent surface above the wide barrier. The bottom graph (b) presents a detail of the wave evolution from Fig. 4. The arrow calls attention to the larger pilot-wave dislocation when the midcavity is present.

related to Fig. 4, is displayed for the same short time interval. This is the case with the presence of the midcavity. As indicated by the arrow, note that in this case the wave has more freedom within the cavity with a quite intense sloshing. By sloshing we mean the lateral movement of the wave, which does not configure propagation. The cavity is too tight for the modulated pilot-wave propagation. Note that when the droplets are isolated at the onset (top graph), the sloshing is very mild. Through the lateral sloshing, the pilot wave acquires momentum. When the impedance to lateral sloshing abruptly increases, the wave steepens as indicated in Fig. 8, to be discussed next. In another striking feature, through the vibrational forcing and droplet bouncing, the enhanced energy of the wave-particle system is sustained beyond isolation. Longer runs were performed, and no decay was evident for $t < 2000T_F$.

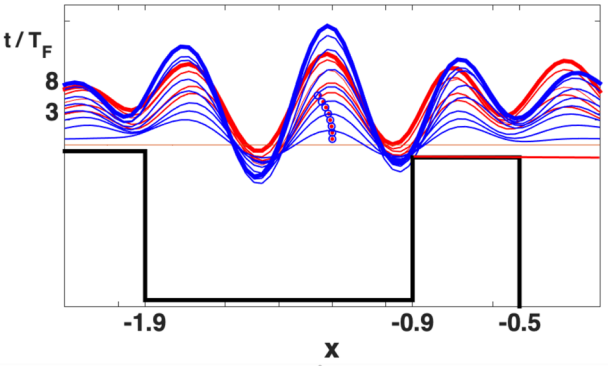

FIG. 8. The isolation process takes place after three Faraday periods. A detail of the leftmost cavity is presented. The wave profiles of the two different cavity systems are superimposed for a total of eight Faraday periods. In red we have a waterfall display of the wave profile in the three-cavity system, while it is in blue when isolation takes place. The last profiles are displayed in a thicker line. The wave elevation is exaggerated for a better visualization and shifted upwards (in time) due to the waterfall display. Half of the midcavity is seen to the right ($-0.5 < x$). The corresponding droplet displacements are given by dots (red) and circles (blue) for the case with isolation. The sudden depth reduction, due to the appearance of the wide barrier [indicated by the horizontal (red) line along $-0.9 < x$], promotes wave steepening and an amplitude increase.

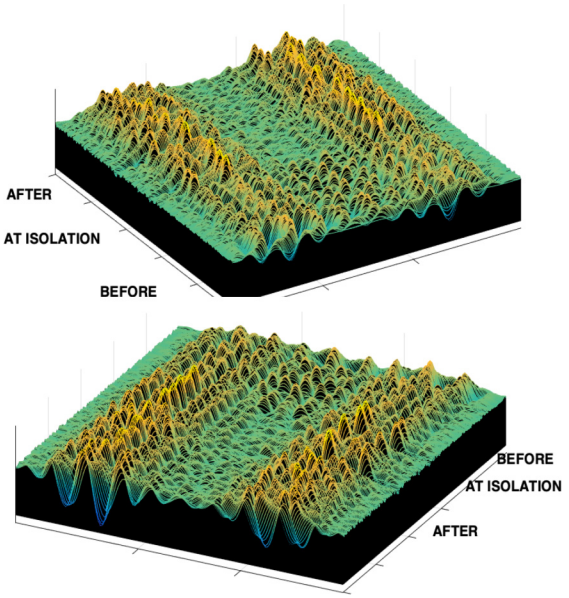

FIG. 9. The wave field for the simulation presented in Fig. 4. The quiescent side regions were removed to highlight the active region. At the top is displayed the "front view," from times just before isolation has been imposed until a bit later beyond isolation. This is a better view to observe the increase of wave amplitude after isolation. At the bottom is displayed the "back view" for the same time interval. This is a better view to see the sharp decrease of wave activity in the middle region where the wide barrier suddenly appeared.

Now we closely observe the effect due to the sudden increase of impedance over the barrier. The acquired momentum during the more intense sloshing will produce a compression of the pilot-wave, hence increasing its slope and therefore further accelerating the droplet. We perform two very short simulations. Each simulation runs for only eight Faraday periods, which are displayed in Fig. 8. In one case we have the presence of the midcavity at all times (red profiles). In the other simulation we set the droplets into isolation after $t = 3T_F$. These two simulations are superimposed in Fig. 8 and help to understand the surprising (very quick) transition to a higher energy level by the particles. Note that the three first wave profiles, and droplet positions, are obviously the same. These are displayed at every Faraday period, in a waterfall fashion being shifted upwards as time evolves. At the third Faraday period, droplet isolation takes place by removing the midcavity and inserting a wide barrier. In the fourth Faraday period displayed, a wave mismatch is observed due to the steepening of the wave field in reaction to the very wide barrier that suddenly appears and enhances the impedance of wave transmission towards the center of the domain. Wave steepening (in blue) quickly accelerates the droplet, through Eq. (8). In the presence of larger wave slopes, more energy is transferred to the oscillator, increasing its range of oscillation. In Fig. 8 one clearly sees the isolated droplet (blue dot) moving faster towards the left. The wave structure and the effect of the wide barrier are further detailed in Fig. 9. This figure presents a three-dimensional (3D) time history of the wave elevation. The vertical scale has been exaggerated for a better visualization. We have removed the side regions of the domain where there is negligible wave activity. Two different views of this wave history are displayed so that the effect of isolation is better observed. From the "front view" the wave height increase (after isolation) is clearly seen along the sides, as shown at the top of Fig. 9. The front vertical plane highlights the first wave profile in this time interval. The sudden communication attenuation due to the barrier can be seen from the "back view," showing less wave activity in the midregion of

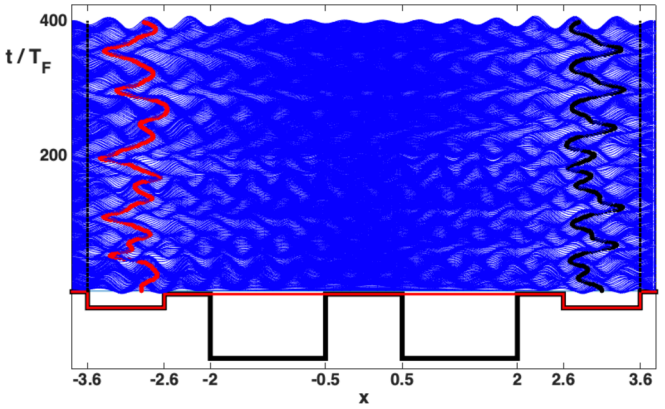

FIG. 10. A four-cavity system with a forcing amplitude of $\Gamma = 4.55$. The dynamics is the same as presented in Nachbin [9]. At time $t = 200T_F$ the two midcavities are replaced by a wide shallow barrier, as indicated by the thin line in the interval $x \in [-2.6, 2.6]$. At this time the magnitude of the vibrational forcing is reduced to $\Gamma = 3.8$. The range of droplet oscillations is effectively unchanged. The wave field over the barrier region is reduced. A more detailed view is presented in Fig. 12.

the cavity system. In particular, the black vertical cut clearly displays less wave activity in the middle.

B. A four-cavity system

Next we consider two droplets separated further apart. We have a four-cavity system (Fig. 10), where droplets can be correlated at a distance through the underlying wave field. The droplets are separated by 5.95 cm, more than 12 Faraday wavelengths apart. Here we consider the same geometry and parameters used in Nachbin [9]. The four-cavity geometry, displayed in Fig. 10, is changed abruptly at $t = 200T_F$. The two midcavities are suddenly replaced by a very long and shallow barrier, as represented by the thin horizontal (red) line. The simulation starts with a shaking strength higher than in the previous case (with $\Gamma = 4.55$) due to the large distance between the oscillators. Shortly after isolation, surprisingly the numerical model becomes Faraday unstable. The mathematical model is linear and has to operate below the Faraday threshold. We noticed that independently of the droplet-isolation time, the wave field would grow indefinitely and the linear approximation would no longer be valid. This was not observed in the three-cavity case. In the present four-cavity case, the isolating process somehow pushes the wave dynamics beyond the Faraday instability threshold (locally). There is no theory to account for this local sudden change of stability.

In the Appendix this novel instability is further detailed. In order to proceed with the droplet dynamics, beyond isolation we concomitantly reduce the strength of the vertical shaking. Hence at $t = 200T_F$, we reduce the strength of the vertical acceleration from $\Gamma = 4.55$ to $\Gamma = 3.8$. The result is presented in Fig. 10. The range of oscillation of both droplets is effectively unchanged, even after isolation and after reducing the shaking to 84% of its initial strength. This is clearly seen in Fig. 11, where we display the orbit of the right droplet in phase space. The starting point is the red dot, and the rectangular marker indicates where isolation takes place. The range of oscillations before and after isolation is mainly the same.

Figure 12 has the 3D time history of the (1D) wave elevation. The figure presents a back view, with later times seen in the foreground. Through the black vertical plane, facing the reader, we observe the higher wave elevation in the two extreme cavities and the lower wave profile in the middle, over the wide barrier. The white dashed line indicates the time of isolation. Prior to isolation (behind the dashed line) the wave activity in the midregion was more intense. Once the wide barrier

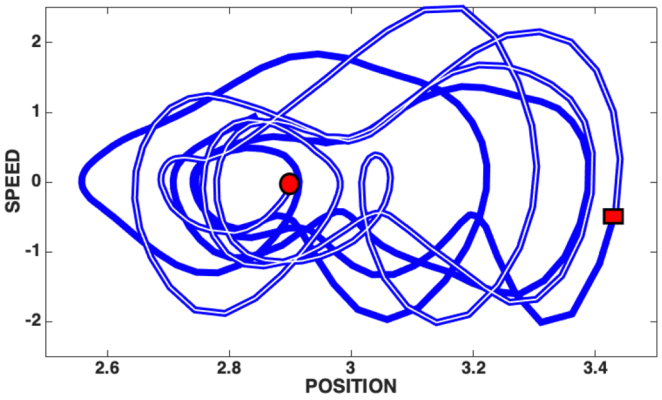

FIG. 11. The phase-space dynamics of the rightmost droplet, regarding the simulation presented in Fig. 10. The dot represents the orbit's initial position, while the rectangle indicates when isolation takes place. Even with the reduction of the shaking strength Γ to 84% of its initial value, after isolation the range of oscillation remained effectively unchanged. When isolated at the onset, the droplets barely oscillate (cf. Fig. 14).

has been introduced (at $t = 200T_F$), the wave field in the central region is substantially reduced. The wide barrier is effective in strongly diminishing the communication between the two oscillators.

The striking result presented in Fig. 6 is again observed even with a greater separation between particles. In Fig. 13 the particles are viewed in phase space through their respective histograms. The top histogram is for the left droplet, and again it has been reflected to the positive axis for a better comparison with the next histogram, which is for the right droplet. Their positions and speeds have been binned in phase space up to the time of isolation ($t = 2000T_F$). After isolation, and the sudden reduction in Γ, both droplets quickly transition to a new and identical probability distribution, as indicated by the two histograms in the lower part of Fig. 13. Their spatial range has not changed much, even under the effect of a sudden forcing reduction. Again we have evidence of information being stored in the wave field during the preisolation dynamics. The transition of probability distributions is faster than any possible signaling between particles, now with the droplets separated by a large distance.

We again verify that, after isolation, the dynamics is energetically much higher than if isolation was set at the beginning of the simulation. When isolation is imposed at the onset, the droplets perform small amplitude oscillations, as can be seen in Fig. 14. The shaking acceleration is $\Gamma = 3.8$, and there is effectively no wave-field activity over the wide barrier, as shown in the bottom part of

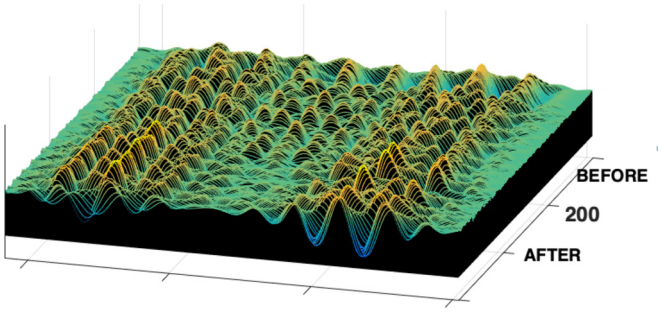

FIG. 12. The wave field for the simulation presented in Fig. 10. The "back view" for a time interval about the isolation moment $t = 200T_F$. A decrease of wave activity is observed in the middle region, where the very wide barrier suddenly appears.

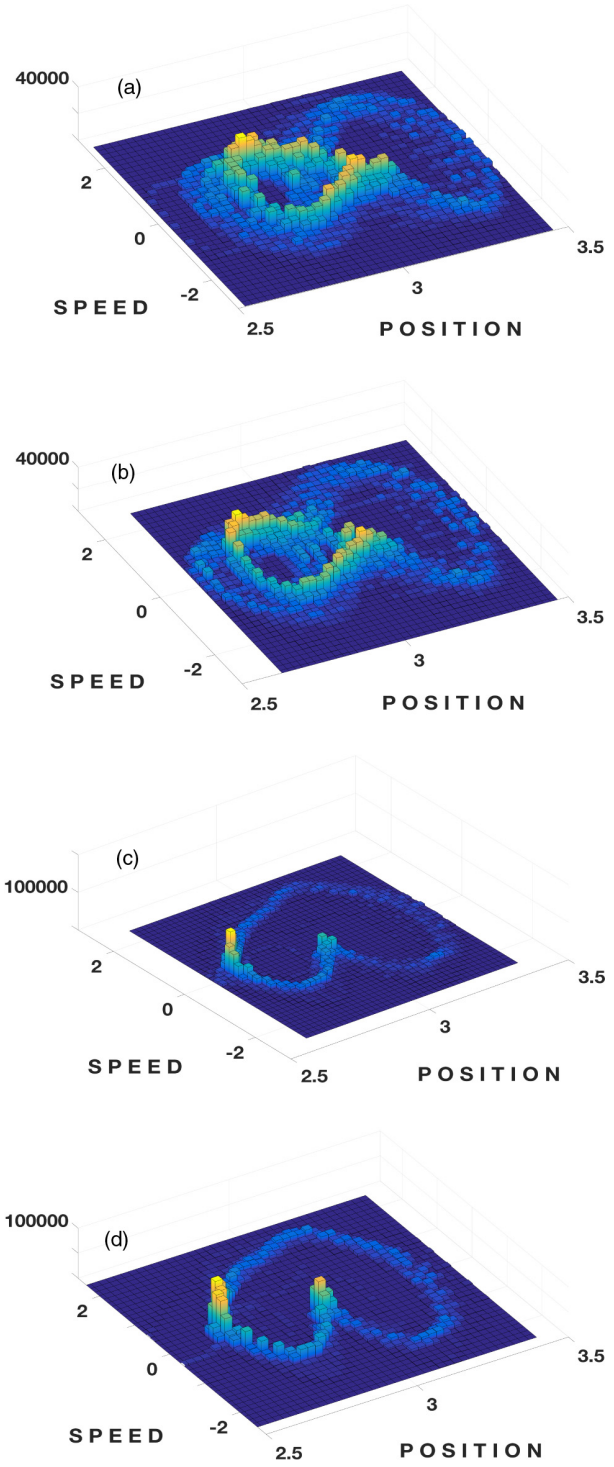

FIG. 13. Histograms in phase space related to a longer run as in Fig. 10. Top two histograms: left (a) and right (b) droplet up to the isolation time $t = 2000T_F$. Bottom two histograms: left (c) and right (d) droplet after isolation and up to time $t = 4000T_F$. After isolation new and identical distributions arise.

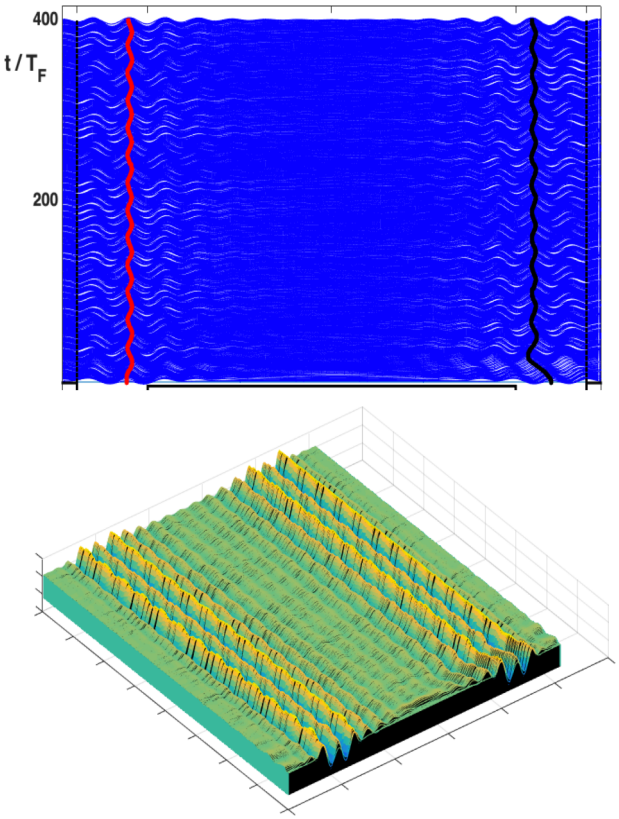

FIG. 14. In Fig. 10 the droplets were isolated at time $t = 200T_F$. Here the droplets are isolated at the onset, and the magnitude of the vertical forcing is set to $\Gamma = 3.8$. At the top the simulation displays very small oscillations by both droplets. The bottom graph presents the 1D wave-elevation history in time. The sides have been trimmed for a better visualization. The front panel shows the wave elevation after 1 Faraday period, and in particular, how the right pilot wave adjusts itself from the center of the cavity to the respective oscillatory location. The nearly quiescent wave field over the wide barrier corroborates the fact that the oscillators are effectively isolated.

Fig. 14. This is an example where energy dissipation and energy production are well balanced, leading to a well-defined harmonic-oscillator-like particle dynamics. In phase space we see a well-defined limit cycle, and its respective histogram as displayed in Fig. 15. The pair (position, speed) is uniformly distributed along the limit cycle. The limit cycle is quite small, in the region [2.83, 2.88]×[-0.3,0.3] of the phase space. On the other hand, when the particles have a prior bipartite experience, after isolation their oscillation is at a much larger range, and this higher energy level is sustained beyond isolation.

IV. CONCLUSION

Two particles (droplets) are allowed to interact for a certain period of time and then are set into isolation. This scenario is inspired by the entanglement experiments in quantum mechanics, as reported by Aspect *et al.* [10]. The wave-mediated particle interaction depends on the cavity structure of the domain. The cavity that traps the droplet plays the role of a potential well. It is shown that particles isolated at the onset have a quite different dynamics then when isolation takes place after some interaction. The underlying wave field, defined on the entire domain, retains shared

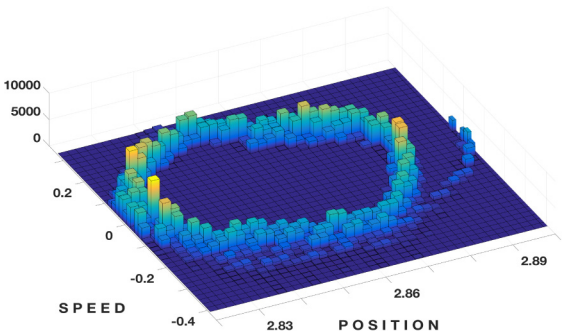

FIG. 15. The histograms for particle X_1 in phase space, related to Fig. 14 but for a longer run up to time $t = 4000T_F$. The number of time steps is indicated on the vertical axis. We have (approximately) a uniformly distributed PDF over the limit cycle.

information from the early interaction period. The bipartite dynamics is therefore nonseparable for all times, with an intrinsic statistical correlation beyond isolation. It has been shown that at the moment of isolation both particles very quickly transition to a new and identical configuration in phase space. There is no possible signaling time between the two particles. This fast statistical transition is induced by the underlying hydrodynamic pilot-wave memory established through preexisting correlations. The new higher energy level is persistent, even in the presence of viscous damping and of the enhanced wave-propagation impedance due to the inclusion of a wide barrier.

As future directions we intend to further study issues related to the nonseparability of the bipartite system, as a follow-up of the present study and of a recent work with collaborators [11]. Nonseparability and intrinsically related correlations hint at the plausibility of performing a hydrodynamic analog of Bell tests and verifying a hydrodynamic analog of entanglement [10].

ACKNOWLEDGMENTS

The author was supported by CNPq under (PQ1D) 307078/2021-3 and FAPERJ Cientistas do Nosso Estado project E-26/201.156/2021.

APPENDIX

1. The maximum phase speed

Benjamin and Ursell [17] studied the linear Faraday instability problem using potential theory. In their analysis a container with inviscid fluid is vertically vibrated at frequency ω_0 in the absence of a droplet. The analysis is reduced to a Mathieu equation. The most unstable mode of the underlying Laplacian is subharmonic, with frequency $\omega_0/2$. In the absence of vibration and droplet forcing, the free motion's dispersion relation is given by

$$\omega^2(k) = kg\tanh(kh_0)\left(1 + \frac{\sigma}{\rho g}k^2\right). \tag{A1}$$

It has been noticed [3,14] that even under the various forcing this dispersion relation is satisfied. The Faraday wave's frequency is $\omega = \omega_0/2$, and solving the dispersion expression for k provides the corresponding Faraday wavelength λ_F. Hence as the Faraday threshold Γ_F is crossed from below a subharmonic wave appears with a wavelength λ_F. See Bush [3] and references within for a detailed account on Faraday waves and related laboratory images. The present pilot wave is generated within the cavity of depth $h_0 = 0.5$ cm. For a vibrational forcing at 80 Hz, the Faraday wavelength is $\lambda_F = 2\pi/k_F \approx 0.47$ cm ($k_F \approx 13.4\,\mathrm{cm}^{-1}$). The respective physical parameters were provided at the beginning of the Results section.

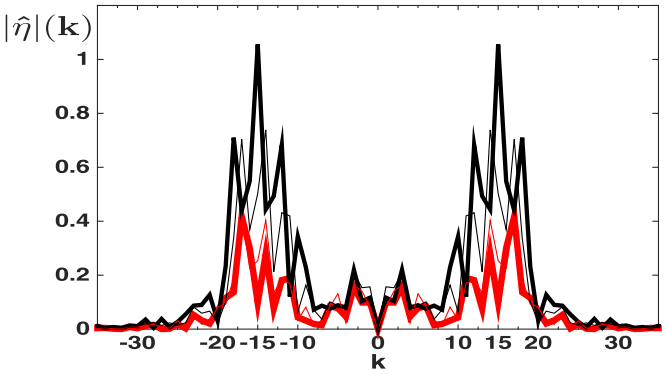

FIG. 16. Fourier spectrum for the wave elevation η over the entire domain, as in the three-cavity simulation of Fig. 4. The red thick line refers to time $t = 399T_F$ just before the wide barrier is introduced. The thin red line, at time $t = 100T_F$, indicates that the spectrum was at the same level prior to isolation. The thin black line is for time $t = 700T_F$, while the thick black line is for time $t = 800T_F$. Both indicate the higher energy level after isolation but within the same bandwidth.

Eddi *et al.* [14] performed laboratory experiments with physical parameters close to those used in the present paper. Their cavity depth is $h_0 = 4.1$ mm, while the silicon oil has surface tension $\sigma = 0.0209$ N/m and density $\rho = 965\,\mathrm{kg/m^3}$. The Faraday wavelength is the same. Inside their main cavity the dispersion relation yields the phase speed $C_F = 18.9$ cm/s, where $C_F = \omega/k_F$. They report that the main crest of the pilot wave moves at the phase speed. In our case the Faraday phase speed is $C_F = 19$ cm/s.

In our present study it is actually important to compute the phase speed over the wide shallow barrier, which is used to isolate the droplets. The depth of this shallow layer is $h_0 = 0.04$ cm. Hence, over the wide barrier the Faraday phase speed is $C_F \approx 13.2$ cm/s. Consider the simulation presented in Fig. 4 with three cavities. Using an FFT, the pilot wave's band-limited spectrum is depicted in Fig. 16. Its bandwidth does not change after the wide barrier is introduced. We noticed in Fig. 4 that the range of the droplets' oscillations increased. In Fig. 16 we observe that the dominant mode's amplitude increases. Somehow energy from the shaking gets further transferred into the cavity modes. The highest mode of the spectrum is about $k = 19$, the rest being roundoff error. The phase speed of this mode is $C_{19} \approx 17.25$ cm/s.

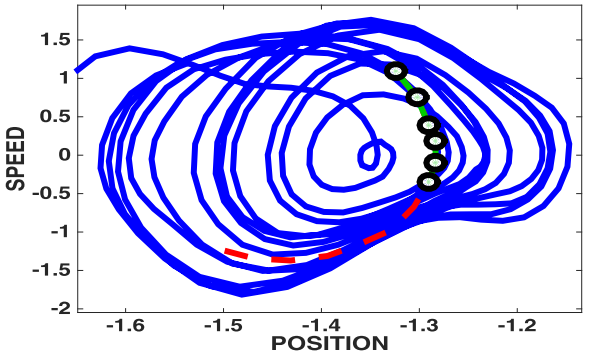

FIG. 17. Phase-space orbit for the left droplet of the three-cavity simulation in Fig. 4. The first white dot is at the time the barrier appears. Each dot is separated by 1 Faraday period. After five Faraday periods the (dashed) orbit is different from that had the barrier not been imposed.

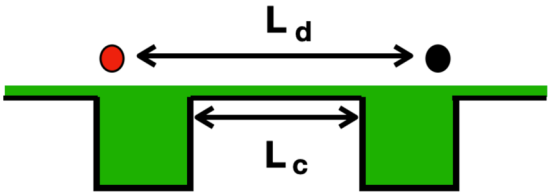

FIG. 18. Schematic picture at the time of isolation when a wide barrier of length L_c is introduced. The distance between droplets is denoted by L_d. These lengths are used to verify the time needed for particles to affect each other after isolation.

By examining the phase plane orbits in Fig. 17, we observe a clear change of particle trajectory after the time of isolation, namely, five Faraday periods later. For simplicity we consider only the left droplet. In the figure the first dot is at the time where the topography is changed. The dots are spaced by a Faraday period. The dashed line indicates the orbit's deviation from the case where the topography had not been changed. Over the time interval of $5T_F = 0.125$ s, a Faraday mode could only travel over the barrier by a distance of $L = 13.2 \times 0.125 = 1.65$ cm. The highest mode observed in the spectrum ($k = 19$) could travel a distance of $L = 17.25 \times 0.125 = 2.16$ cm. Using the schematics of Fig. 18, the distance between cavities is $L_c = 1.8$ cm. At time $t = 400T_F$, the time of isolation, the distance between droplets was $L_d = 2.56$ cm. At time $t = 405T_F$, when the phase-space trajectories differ, the distance between droplets is $L_d = 2.50$. Therefore there was not enough time for one droplet to affect the other during the five Faraday periods after the wide barrier was introduced.

For the four-cavity case, the left droplet's phase-space orbit is depicted in Fig. 19. The large white dot indicates the time when the topography is changed as well as the vibrational forcing. After two Faraday periods the orbit has already deviated from the case without a topographic change. The wave's Fourier spectrum is shown in Fig. 20, and we observe that the effective amplitudes and bandwidth are unchanged. The droplets in this case are further apart. Hence there is no time for a droplet to affect the other before changes are observed in the phase-space orbits and in the respective histograms.

2. The Faraday threshold

As mentioned in the Introduction, a subharmonic wave instability takes place when $\Gamma \geqslant \Gamma_F$ [4,17], where Γ_F is the Faraday threshold. The Faraday threshold for a complex cavity system, as

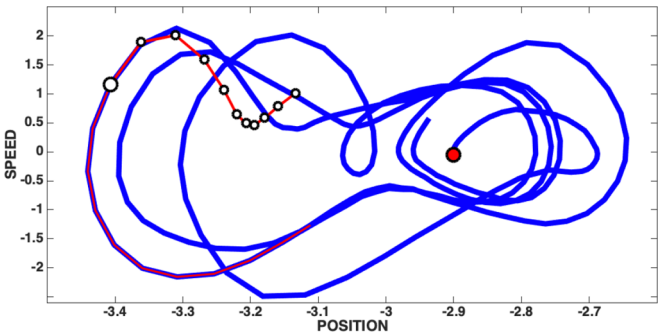

FIG. 19. Phase-space orbit for the left droplet of the four-cavity simulation in Fig. 10. The red dot indicates the initial position. The larger white dot is at the time the wide barrier appears. The dots are separated by one Faraday period.

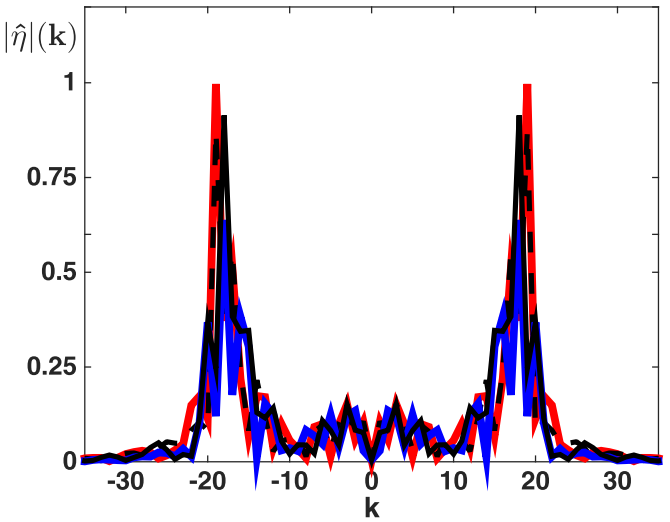

FIG. 20. Fourier spectrum for the wave elevation η over the entire domain, as in the four-cavity simulation of Fig. 10. The red line refers to time $t = 199T_F$, just before the wide barrier is introduced with forcing at $\Gamma = 4.55$. The black, blue, and dashed lines are respectively at times $t = 201T_F$, $220T_F$, $240T_F$, after the barrier was introduced at time $t = 200T_F$ and the forcing reduced to $\Gamma = 3.8$.

used in our study, can only be found numerically. For example, changing barrier heights or widths changes the instability threshold. Even when the vibrational forcing is $\Gamma < \Gamma_F$, a bouncing droplet can trigger the most unstable mode, but this mode will not grow. Hence to find the Faraday threshold we allow the droplet to bounce once, over our prescribed contact time, and observe the evolution of the Faraday wave generated. If the Faraday wave generated decays, we are below the instability threshold. We then increase the value of Γ until the respective Faraday wave grows in time. This is clearly seen in Figs. 21 and 22. In Fig. 21 we have $\Gamma = 4.55$, as used in the four-cavity geometry presented in Fig. 10. The black dot indicates the position where the droplet does its single bounce. At the end of the first Faraday period we highlight the Faraday wave generated. We observe a transient propagating away in both directions and vanishing, while the standing Faraday wave profile decays in time and is quite small after 25 Faraday periods (at $t = 25T_F$). When the vibrational forcing

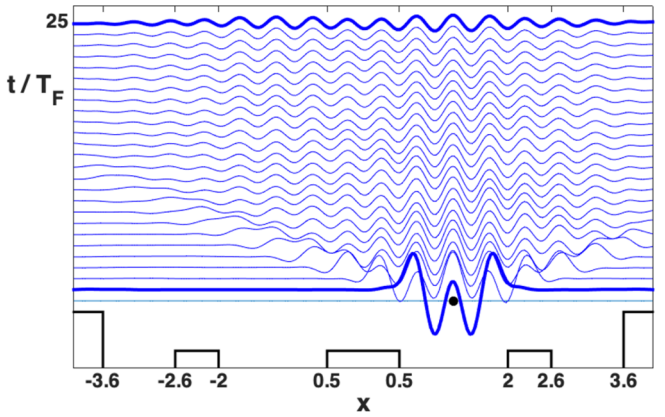

FIG. 21. The numerical Faraday instability test with a vibrational forcing of $\Gamma = 4.55$. This case is stable since the initial disturbance decays in time.

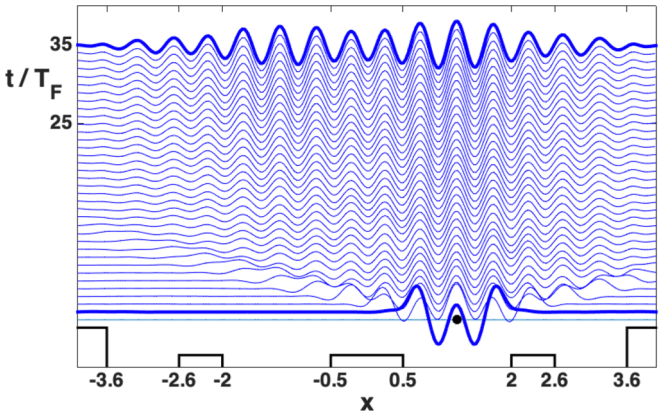

FIG. 22. The numerical Faraday instability test with a vibrational forcing of $\Gamma = 4.70$. This case is unstable since the initial disturbance grows in time.

reaches $\Gamma = 4.70$, the Faraday wave becomes unstable, and this defines the Faraday threshold as $\Gamma_F = 4.70$. In Fig. 22 we observe the steady growth of the wave field, which ends up extending over the entire domain. We point out that it did not matter if the droplet's bounce was taken in the rightmost cavity, as shown, or in the deeper midcavity. The threshold was the same. But the growth rate in the deeper cavity is larger. As pointed out in Nachbin [9], the midcavity was designed to function as a nearly resonant signal amplifier, thus enhancing long-range correlations.

The simulation presented in Fig. 10 started at 97% of the threshold value. In the presence of the wide barrier the Faraday threshold becomes higher due to the large shallow region, which

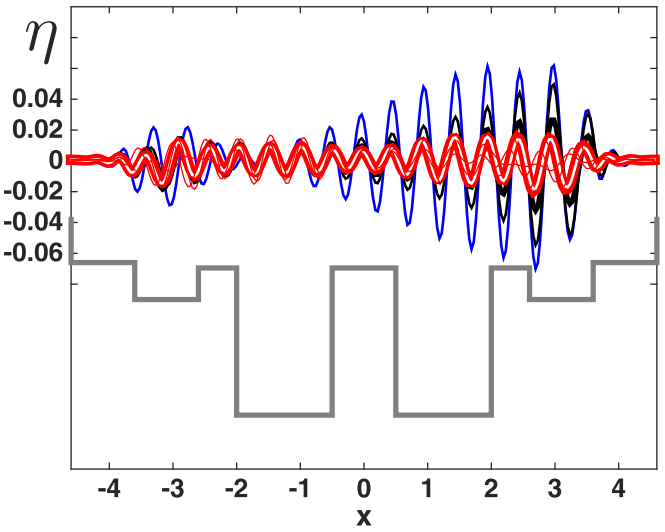

FIG. 23. The wave elevation, from the simulation of Fig. 10, just before and after a new Faraday instability takes place. The cavity system is depicted out of scale to provide a reference for the wave location. The red thick line shows $\eta(x, 199T_F)$, while the thin (red) line shows the previous times $t = 185T_F, 190T_F, 195T_F$. The thin white line, coinciding with the red curve, is at the isolation time $t = 200T_F$. Just after the wide barrier is introduced, we observe a steady growth of the wave elevation depicted at times $t = 202T_F$ (thick black), $205T_F$ (thin black), and $210T_F$ (blue). The corresponding Fourier spectrum is presented in Fig. 24.

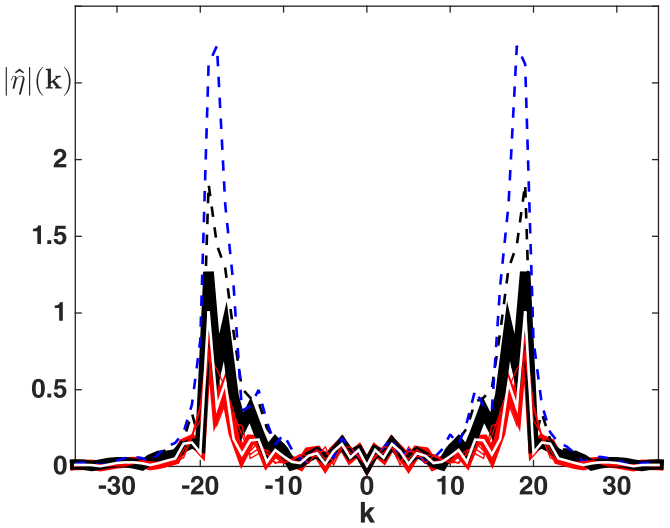

FIG. 24. Fourier spectrum for the wave elevation for the profiles of Fig. 23. The red line refers to $t = 199T_K$, while the white line refers to the isolation time $t = 200T_K$. The thick black line is the spectrum at time $t = 202T_F$, while the dashed lines respectively show times $t = 205T_F,\ 210T_F$.

necessarily attenuates the Faraday waves. We found the instability threshold to be at $\Gamma_F = 5.15$, using a similar procedure to that described above. In Fig. 10, as the barrier was suddenly introduced we had to reduce the vibrational forcing to $\Gamma = 3.8$, namely, to 74% of the respective wide-barrier threshold. This forcing reduction was enforced in order to avoid a new, modified Faraday instability threshold, as is now discussed.

If we had not reduced the vibrational forcing, immediately after the introduction of a wide barrier the wave elevation would develop an instability as depicted in Fig. 23. The barrier was introduced at time $t = 200T_F$. At $t = 199T_F$ the wave elevation over the entire domain is represented by the thick red line, while $t = 200T_F$ is shown by a thin white line very similar to the previous profile. Three thin red lines display the wave elevation at earlier times ($t = 185T_F,\ 190T_F,\ 195T_F$). They are not depicted in detail because the point is to show that their amplitudes are all of the same order. When the barrier is introduced, the wave elevation grows indefinitely, as respectively depicted at

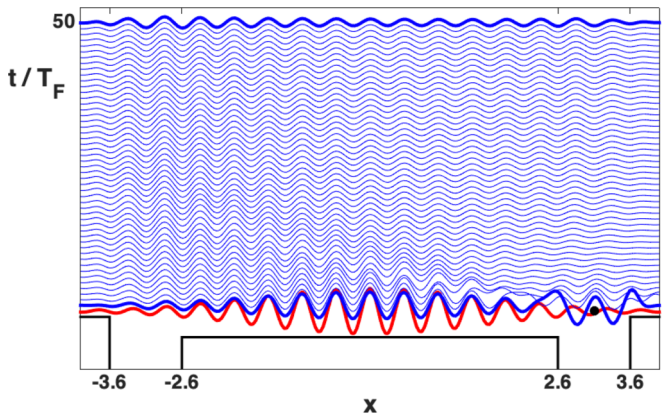

FIG. 25. The numerical Faraday instability test with a background elevation at $k_D = 13.4$ ($\Gamma = 5.0$).

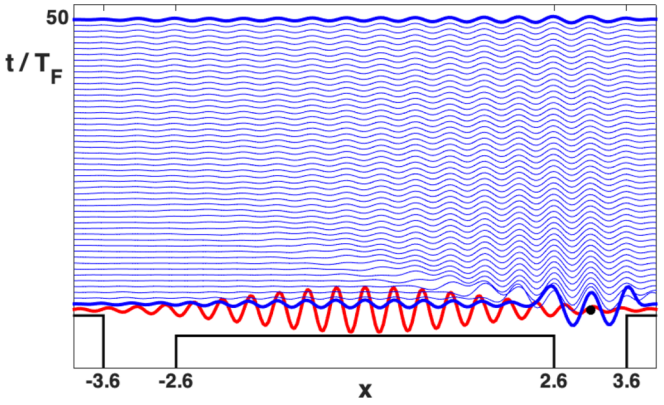

FIG. 26. The numerical Faraday instability test with a background elevation at $k_D = 16$ ($\Gamma = 5.0$).

times $t = 202T_F,\ 205T_F,\ 210T_F$. This secondary instability manifests itself first over the region of the right cavity. Then it also slowly manifests itself over the left cavity. The growth is triggered by the dominant Faraday mode (see Fig. 24). Through the FFT one clearly sees that the instability is predominantly monochromatic, centered on the dominant mode. All modes outside the effective wave-number band are stable. The sudden change in the cavity configuration and very likely the sloshing compression, reported earlier, trigger this Faraday instability not seen before in pilot-wave dynamics. There is yet no theory to predict this sudden growth.

Therefore we provide a preliminary rationalization of this instability through computational simulations. The standard Faraday instability occurs about an undisturbed free surface. The observed instability takes place in the presence of a long-wave mode and seems to be connected with the sudden increase of impedance against sloshing. This promotes its steepening, as demonstrated in Fig. 8, and the droplet's continuous bouncing triggers this secondary instability. This has not been studied before, is beyond the scope of the present work, and deserves further understanding. The above explanation, while preliminary and speculative, motivated the following simulations along the lines of the Faraday instability test.

In the following Faraday instability test, rather than having a flat undisturbed surface, we consider a preexisting long-range background disturbance. We choose the preexisting stationary surface disturbance $\eta_0(x) = 0.008\exp(-0.2x^2)\cos(k_D x)$, which resembles the above long-range mode. First, take a disturbance having exactly the Faraday wave number with $k_D = 13.4$ and ranging over

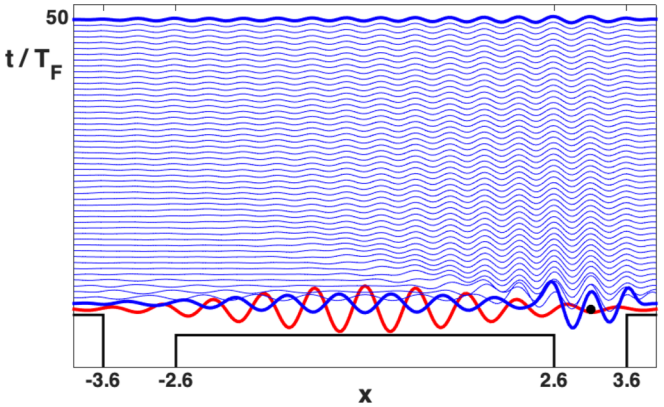

FIG. 27. The numerical Faraday instability test with a background elevation at $k_D = 9$ ($\Gamma = 5.0$).

the wide barrier. The vibrational forcing is $\Gamma = 5.0$. The Faraday instability test with the single droplet bounce is presented in Fig. 25. The presence of the long-range disturbance sustained the effect of the single bounce for much longer time than if it had taken place in the standard flat-surface case. Note that over the other cavity (to the left) the wave field is being sustained for even longer than where the bounce took place. The fact that the preexisting long-range disturbance has the Faraday wavelength is important. Changing the wave number k_D of the background disturbance affects the dissipation rate of the droplet's single bounce. In Fig. 26 the background disturbance has $k_D = 16$, while in Fig. 27 it has $k_D = 9$. In both cases the background disturbance did not help to sustain the wave field for a longer period of time, and it did not transfer information to the other cavity as it did for the subharmonic mode case $k_D = 13.4$.

[1] Y. Couder, S. Protière, E. T. Fort, and A. Boudaoud, Walking and orbiting droplets, Nature (London) **437**, 208 (2005).

[2] Y. Couder and E. T. Fort, Single-Particle Diffraction and Interference at a Macroscopic Scale, Phys. Rev. Lett. **97**, 154101 (2006).

[3] J. W. M. Bush, Pilot-wave hydrodynamics, Annu. Rev. Fluid Mech. **47**, 269 (2015).

[4] J. W. M. Bush and A. U. Oza, Hydrodynamic quantum analogs, Rep. Prog. Phys. **84**, 017001 (2021).

[5] J. W. M. Bush, Y. Couder, T. Gilet, P. A. Milewski, and A. Nachbin, An introduction to focus issue on hydrodynamics quantum analogs, Chaos **28**, 096001 (2018).

[6] R. Horodecki, P. Horodecki, M. Horodecki, and K. Horodecki, Quantum entanglement, Rev. Mod. Phys. **81**, 865 (2009).

[7] R. F. Werner, Quantum states with Einstein-Podolsky-Rosen correlations admitting a hidden-variable model, Phys. Rev. A **40**, 4277 (1989).

[8] J. Henson, Non-separability does not relieve the problem of Bell's theorem, Found. Phys. **43**, 1008 (2013).

[9] A. Nachbin, Walking droplets correlated at a distance, Chaos **28**, 096110 (2018).

[10] A. Aspect, P. Grangier, and G. Roger, Experimental Realization of Einstein-Podolsky-Rosen-Bohm, *Gedankenexperiment*: A New Violation of Bell's Inequalities, Phys. Rev. Lett. **49**, 91 (1982).

[11] K. Papatryfonos, M. Ruelle, C. Bourdiol, A. Nachbin, J. W. M. Bush, and M. Labousse, Hydrodynamic superradiance in wave-mediated cooperative tunneling, Commun. Phys. **5**, 142 (2022).

[12] K. Papatryfonos, L. Vervoort, A. Nachbin, M. Labousse, and J. W. M. Bush, Bell test in a classical pilot-wave system, arXiv:2208.08940.

[13] J. Acebrón, L. Bonilla, V. Perez, F. Ritort, and R. Spigler, The Kuramoto model: A simple paradigm for synchronization phenomena, Rev. Mod. Phys. **77**, 137 (2005).

[14] A. Eddi, E. Sultan, J. Moukhtar, E. Fort, M. Rossi, and Y. Couder, Information stored in Faraday waves: The origin of a path memory, J. Fluid Mech. **674**, 433 (2011).

[15] P. A. Milewski, C. A. Galeano-Rios, A. Nachbin, and J. W. M. Bush, Faraday pilot-wave dynamics: Modelling and computation, J. Fluid Mech. **778**, 361 (2015).

[16] A. Nachbin, P. A. Milewski, and J. W. M. Bush, Tunneling with a hydrodynamic pilot-wave model, Phys. Rev. Fluids **2**, 034801 (2017).

[17] T. B. Benjamin and F. J. Ursell, The stability of the plane free surface of a liquid in vertical periodic motion, Proc. R. Soc. Lond. A **225**, 505 (1954).

[18] T. A. Driscoll and L. N. Trefethen, *Schwarz-Christoffel Mapping* (Cambridge University Press, England, 2002).

[19] A. Nachbin, A terrain-following Boussinesq system, SIAM J. Appl. Math. **63**, 905 (2003).

[20] A. Fokas and A. Nachbin, Water waves over a variable bottom: A non-local formulation and conformal mappings, J. Fluid Mech. **695**, 288 (2012).

[21] A. Nachbin, Kuramoto-like synchronization mediated through Faraday surface waves, Fluids **5**, 226 (2020).

[22] L. de la Peña, A. M. Cetto, and A. V. Hernández, *The Emerging Quantum* (Springer, Switzerland, 2015).